SCIENTIFIC REPORTS

OPEN

SUBJECT AREAS:
PERMEATION AND TRANSPORT
MICROSCOPY
BLOOD FLOW
FLUORESCENCE IMAGING

Received
23 September 2014

Accepted
17 November 2014

Published
5 December 2014

Correspondence and requests for materials should be addressed to L.S. (laura.sironi@unimib.it) or G.C. (Giuseppe.Chirico@mib.infn.it)

* These authors contributed equally to this work

In Vivo Flow Mapping in Complex Vessel Networks by Single Image Correlation

Laura Sironi[1]*, Margaux Bouzin[1]*, Donato Inverso[2,4], Laura D'Alfonso[1], Paolo Pozzi[1], Franco Cotelli[3], Luca G. Guidotti[2], Matteo Iannacone[2,4], Maddalena Collini[1] & Giuseppe Chirico[1]

[1]Università degli Studi di Milano-Bicocca, Physics Department, Piazza della Scienza 3, I-20126, Milan, Italy, [2]Division of Immunology, Transplantation and Infectious Diseases, IRCCS San Raffaele Scientific Institute, I-20132, Milan, Italy, [3]Università degli Studi di Milano, Department of Life Sciences, Via Celoria 26, I-20133, Milan, Italy, [4]Vita-Salute San Raffaele University, I-20132, Milan, Italy.

We describe a novel method (FLICS, FLow Image Correlation Spectroscopy) to extract flow speeds in complex vessel networks from a single raster-scanned optical *xy*-image, acquired *in vivo* by confocal or two-photon excitation microscopy. Fluorescent flowing objects produce diagonal lines in the raster-scanned image superimposed to static morphological details. The flow velocity is obtained by computing the Cross Correlation Function (CCF) of the intensity fluctuations detected in pairs of columns of the image. The analytical expression of the CCF has been derived by applying scanning fluorescence correlation concepts to drifting optically resolved objects and the theoretical framework has been validated in systems of increasing complexity. The power of the technique is revealed by its application to the intricate murine hepatic microcirculatory system where blood flow speed has been mapped simultaneously in several capillaries from a single *xy*-image and followed in time at high spatial and temporal resolution.

Microcirculation, a complex network of small vessels with a typical diameter ranging from 5 to 50 μm, delivers nutrient-rich oxygenated blood to tissues and organs, playing a crucial role in their maintenance and hemodynamics[1]. Moreover, it interacts extensively with the immune system and its impairments and dysfunctions lead to several pathological conditions[2–4]. Therefore, mapping the blood flow velocity in microvessels is crucial for the characterization of healthy and diseased organs.

State-of-the-art clinical techniques for measuring the blood flow (Doppler Tomography[5], Magnetic Resonance Imaging[6], Optical Coherence Tomography[7] and Ultrasound Imaging[8]) are not suitable to characterize the microcirculation system since they lack the spatial resolution required to scale down to individual capillaries[9,10].

The recent development of novel fluorescent dyes and of genetically encoded fluorescent proteins[11,12] opened new fields in intravital optical microscopy-related techniques for the study of the blood flow. Among these techniques, Particle Image Velocimetry[13,14], dual-foci cross correlation[15,16] and line-scan measurements[17,18] rely on the measurements of the temporal decay of the fluorescence fluctuations coming from molecules or cells flowing through the observation volume. This is accomplished by applying auto- or cross-correlation methods on temporal stacks of wide field images or on *xt*-images obtained by repetitive line scanning along a vessel.

In spite of the high temporal (~ms) and spatial (~μm) resolution achieved, line scan-based methods[18–21] lack the ability to correlate the flow speed values with the morphological details in an intricate network of capillaries. In this paper, we propose therefore a novel technique (FLICS, FLow Image Correlation Spectroscopy) that, by employing a *single* raster-scanned *xy*-image acquired *in vivo* by confocal or multi-photon excitation fluorescence microscopy, allows the quantitative measurement of the blood flow velocity in the whole vessel pattern within the (large) field of view, while simultaneously maintaining the morphological information due to the immobile structures of the explored circulatory system. This is achieved by computing the cross-correlation function among pairs of columns in selected regions of interest in the *xy*-image. Being based on a single raster scanning acquisition, this procedure can be readily extended to follow the dynamical parameters in time (*xyt*-stacks) or in 3D volumes (*xyz*-stacks).

The description of the proposed method and the explicit analytical expression of the cross-correlation function are followed by validation measurements in the simple circulatory system of Zebrafish embryos. FLICS power is then fully shown by its application to the complex hepatic microcirculatory system in living anesthetized mice. The blood flow is characterized here at the level of individual sinusoids starting from single raster-scanned *xy*-images and is followed versus time.

Results

Cross-correlation on *xy*-images. FLICS relies on single *xy*-images acquired in confocal or two-photon excitation microscopy by *raster* scanning a sample where the fluorescence signal comes from flowing brightly fluorescent objects (genetically modified red blood cells, injected fluorescent beads, quantum dots, etc), which produce in the *xy*-image diagonal lines superimposed to morphological details. The orientation of these diagonal lines with respect to the reference Cartesian *xy*-plane depends on the flow direction relative to the positively *x*-oriented scan path (Fig. 1a–e). The slope and width of the diagonal lines are determined by the image acquisition parameters and by the fluorescent particles properties: size, diffusion coefficient and, most importantly, flow speed $|\underline{v}|$. A key role is played by the scan frequency: horizontal lines are obtained for scan speeds lower than the drift speed, whereas the slope increases when the scan speed is higher than the modulus $|\underline{v}|$. In this case, quantitative information regarding the flow speed can be achieved by computing the Cross-Correlation Function (CCF) of the fluorescence fluctuations detected in pairs of columns of a selected Region Of Interest (ROI) of the *xy*-image where diagonal lines appear. The CCF is defined as the normalized time average of the product of the fluorescence intensity fluctuations detected in the pixels sampled at time t in the first column and at a delayed time $t + \tau$ in the second column. The CCF allows therefore the exploitation of the spatio-temporal information intrinsically enclosed in a single raster-scanned image for the measurement of the blood flow speed. In this regard, FLICS shares the approach of previous image correlation-based methods[22–24] conceived for the investigation of slow diffusive or directional motions of fluorescently labeled macromolecules within the plasma membrane of living cells[25,26].

The definition and derivation of the cross-correlation function rely on the description of a raster-scanned *xy*-image as a matrix of N_xxN_y pixels, each identified by a couple of integer indexes (x, y), with $x \in [0, N_x–1]$ and $y \in [0, N_y–1]$ (Fig. 1f). The pixel of coordinates (x, y) is sampled at time $t = x\tau_{pixel} + y\tau_{line}$ with respect to the pixel in position (0,0), where τ_{pixel} is the pixel dwell time and $\tau_{line} \equiv 1/f_{line}$ is the inverse of the scan frequency per line. This space-time encoding allows to write the fluorescence intensity of the pixels belonging to column x as $F_x(y(t), t)$, using the variable "time" to discriminate the different pixels. The fluctuation $\delta F_x(y(t), t)$ is defined as the deviation of the intensity $F_x(y(t), t)$ from its average computed over the entire column. In this notation, the CCF of the fluorescence intensity fluctuations detected in two columns a fixed distance l apart is given by

$$G_{x,x+l}(\tau) = \frac{\langle \delta F_x(y(t),t)\delta F_{x+l}(y(t+\tau),t+\tau)\rangle_t}{\langle F_x(y(t),t)\rangle_t \langle F_{x+l}(y(t),t)\rangle_t} \qquad (1)$$

The subscripts x and $x + l$ identify the chosen columns and τ is the correlation lag time. We call n the spatial lag along the vertical *y*-direction between the pixel sampled at time t in the first column and the pixel sampled at time $t + \tau$ in column $x + l$. The lag time τ can then be expressed as $\tau = l\tau_{pixel} + n\tau_{line} \cong n\tau_{line}$, where $l\tau_{pixel} \ll n\tau_{line}$ usually holds, especially for small column distances, since pixels are typically a few microseconds apart along the horizontal direction and a few milliseconds apart along the vertical direction. Time averaging is obtained by taking all the pairs of pixels belonging to the two selected columns at a distance $n \sim \tau/\tau_{line}$ apart along the vertical *y*-direction of the image or of the ROI.

The explicit expression of the CCF has been derived in Supplementary Note 1 for two generic columns I and J at distance $l \equiv J–I$ ($I < J$, $I \in [0, N_x–2]$ and $J \in [I + 1, N_x–1]$): it is computed from the fluorescence fluctuations registered in column I at time t and in column J at time $t + \tau$ (forth cross-correlation G_{IJ}) for a positively *x*-oriented vector $\underline{v}$, or from the fluorescence fluctuations

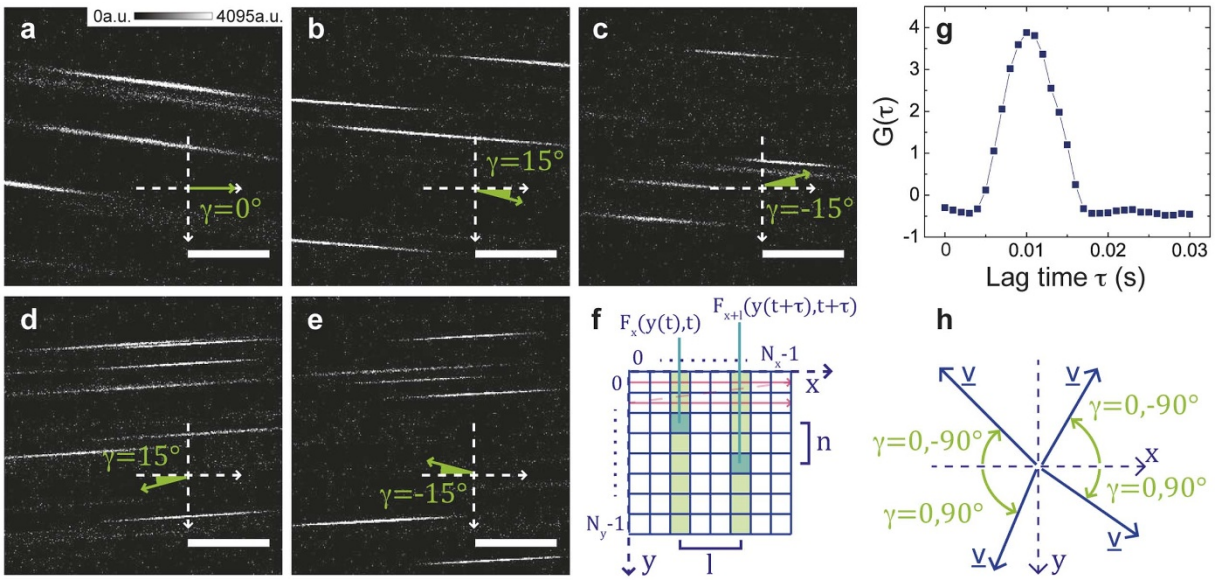

Figure 1 | Cross-correlation on raster-scanned xy-images. (a)–(e) Confocal xy-images acquired by detecting the signal of 1-μm fluorescent beads undergoing laminar flow in a square borosilicate capillary (inner section, 720 μm); λ_{exc} = 514 nm, detection bandwidth = 530–600 nm, f_{line} = 1000 Hz, δx = 0.04 μm; scale bar, 3 μm. The angle γ between the flow velocity vector $\underline{v}$ and the scan path (pointing as the positive x-axis) was varied in the four quadrants of the Cartesian xy-plane. In (a), (b) and (c) $\underline{v}$ (in green) points in the positive x-direction: the diagonal lines due to the beads motion keep the same orientation irrespectively of the angle γ, which affects their length and slope. In (d) and (e) $\underline{v}$ points in the negative *x*-direction (i.e., opposite to the scan path) and the orientation of the diagonal lines is reversed. In each image γ is reported according to the definition of panel (h). (f) A raster-scanned image (or a region of interest) is a matrix of N_xxN_y pixels, representing a series of intensity measurements from many adjacent confocal excitation volumes (sampled along the red pattern). The sketch highlights (dark green) two arbitrary pixels involved in the computation of the forth cross-correlation between two columns (light green) $l = J$-I pixels apart. (g) Exemplary CCF computed on panel (a) for $(J–I)\delta x$ = 7.4 μm. (h) Definition of the angle γ between the vector $\underline{v}$ and the scan axis (positive *x*-axis); the range of its possible values and four arbitrarily-directed vectors for the flow velocity are shown.

detected in column I at time $t + \tau$ and in column J at time t (back cross-correlation G_{JI}) for a negatively x-oriented vector $\underline{v}$ (Fig. 1). For a positive v_x,

$$G_{IJ}(\tau) \propto \frac{1}{\left(4sD\tau + \frac{a^2 s}{2} + \omega^2\right)} \frac{1}{\sqrt{\left(4sD\tau + \frac{a^2 s}{2} + \omega_z^2\right)}} \cdot$$
$$\cdot exp\left\{ - \frac{[(J-I)\delta x - v_x \tau]^2}{\left(4sD\tau + \frac{a^2 s}{2} + \omega^2\right)} \right\} exp\left\{ - \frac{\left[\frac{\delta x}{\tau_{line}} - v_y\right]^2 \tau^2}{\left(4sD\tau + \frac{a^2 s}{2} + \omega^2\right)} \right\} \quad (2)$$
$$exp\left\{ - \frac{v_z^2 \tau^2}{\left(4sD\tau + \frac{a^2 s}{2} + \omega_z^2\right)} \right\}$$

where δx is the pixel size (we assume $\delta x = \delta y$ smaller than half the microscope spatial resolution), $s = 1,2$ for s-photon excitation and ω and ω_z are the laser beam waists along the radial and axial directions, respectively. a is the radius of the flowing objects, which appears explicitly in the CCF expression whenever the objects are larger than the beam waist[27], as in the case of Red Blood Cells (RBCs) in Zebrafish vessels. D is the diffusion coefficient, that must be regarded as an effective value for large flowing objects in small vessels as already reported[28]. In fact, the combined effects of the RBCs size and concentration, of their interaction with the vessel boundaries and of the elastic interaction of these on RBCs result in an effective diffusion coefficient[28] much larger than the Stokes-Einstein's predictions ($\sim$0.1 $\mu m^2/s$).

The z-component of the vector $\underline{v}$ is negligible when the FLICS method is applied to circulatory systems with an approximately planar structure. Both in our calibration measurements in Zebrafish embryos and in our investigation of the hepatic microcirculation, xy-images have been acquired in subunits of the circulatory system where the majority of the vessels (and the velocity vector $\underline{v}$) lie in the same xy-plane sampled by the excitation laser beam. In this case the CCF is a peaked function (Fig. 1g) given explicitly by

$$G(\tau) \propto \propto \frac{1}{\left(4sD\tau + \frac{a^2 s}{2} + \omega^2\right)} \frac{1}{\sqrt{\left(4sD\tau + \frac{a^2 s}{2} + \omega_z^2\right)}}$$
$$exp\left\{ - \frac{[(J-I)\delta x - |\underline{v}|\cos(\gamma)\tau]^2}{\left(4sD\tau + \frac{a^2 s}{2} + \omega^2\right)} \right\} \quad (3)$$
$$exp\left\{ - \frac{\left[\frac{\delta x}{\tau_{line}} - |\underline{v}|\sin(\gamma)\right]^2 \tau^2}{\left(4sD\tau + \frac{a^2 s}{2} + \omega^2\right)} \right\}$$

The angle γ that the planar vector $\underline{v}$ subtends with the horizontal x-axis is defined in Figure 1h: with this definition, equation (3) can be equivalently employed for an either positively or negatively x-oriented vector $\underline{v}$ (Supplementary Note 1 and Supplementary Fig. 1).

The effects produced on the CCF overall shape and on the lag time (τ_{max}) of its maximum by the most relevant parameters, such as the blood flow speed $|\underline{v}|$, the column distance J–I, the scan frequency f_{line} and the angle γ, have been investigated on simulated CCFs (Supplementary Fig. 2). The effect of an increasing flow speed is to shift the peak time τ_{max} toward shorter lag times. The peak of the CCF is in fact directly related to the time it takes, on average, for flowing objects to travel the distance between the columns selected for the CCF derivation. For the same reason, an opposite shift of the peak time τ_{max} toward longer lag times is found when the column distance is increased. The functional dependence of the peak time on the column distance and on the flow speed, as well as on the other image acquisition parameters, is reported in Supplementary Note 2. The scan frequency does not remarkably affect the CCF shape and peak time, but it determines the time axis scaling ($\tau \approx n\tau_{line}$), defining therefore the time resolution in the CCFs sampling. The scan frequencies available on commercial microscopes also determine the range of blood flow speeds that can be measured: the condition $v_{scan} = f_{line}(N_x \delta x) > |\underline{v}|$ leads, for scan frequencies $\sim$10–8000 Hz and for an x-size of the field of view ($N_x \delta x$) $\sim$ 150 μm, to a broad range $|\underline{v}| \lesssim$ 1.2 cm/s of measurable blood speeds. The dependence of the CCF on the angle between the scan path and the flow direction finally highlights the sensitivity of FLICS for blood flow speed measurements for any relative orientation of the scan and flow directions, as will be extensively investigated in the calibration measurements on Zebrafish embryos (Fig. 2). This proofs to be a great advantage for the characterization of intricate capillary networks.

Measurement of the blood flow speed. When working on a ROI of a single xy-image, a total of N_x–(J–I) CCFs are computed and averaged, so that all the columns at a distance (J-I) in the ROI are exploited. Two procedures can then be adopted to obtain the blood flow speed.

The first method requires a *global* fit to equation (3) of a set of experimental CCFs derived for multiple column distances. The flow speed $|\underline{v}|$ and the properties of the flowing objects (radius and effective diffusion coefficient) are always kept as free parameters in the CCFs fit, whereas the optical and scan parameters, ω, ω_z, (J–I), δx and τ_{line} are treated as known quantities. The angle γ is fixed to the value measured from the orientation of the vessel with respect to the x-axis (assuming that fluorophores flow in a direction parallel to the vessel wall, as in our case with RBCs).

The second procedure, which proofs to be much faster, exploits the peak time of the experimental CCFs. In Supplementary Note 2, we derive the analytical expression of the peak time (τ_{max}), which, for vanishing values of the diffusion coefficient, simplifies to

$$\tau_{max}^0 = \frac{(J-I)\delta x |\underline{v}| \cos(\gamma)}{\left[\frac{\delta x}{\tau_{line}} - |\underline{v}|\sin(\gamma)\right]^2 + [|\underline{v}|\cos(\gamma)]^2} \quad (4)$$

By substituting to τ_{max}^0 the experimentally-recovered peak time and inverting equation (4) for the modulus of the flow velocity, we can derive an approximate estimate $|\underline{v}|^0$ of the flow speed. This procedure is repeated for each of the column distances (J–I)δx used in the CCFs derivation and a weighted average of the resulting $|\underline{v}|^0$ values is computed. The weights are provided by the experimental uncertainty on each $|\underline{v}|^0$ value as derived in Supplementary Note 2. The accuracy on this flow speed estimate clearly depends on the validity of the assumption $D = 0$. The relative discrepancy between $|\underline{v}|$ (equation (3)) and $|\underline{v}|^0$ (equation (4)) has been extensively investigated (Supplementary Note 2 and Supplementary Fig. 3) by simulating the ratios τ_{max}/τ_{max}^0 and $|\underline{v}|/|\underline{v}|^0$ as a function of the diffusion coefficient D (0–300 $\mu m^2/s$), for increasing values of the flow speed, of the scan frequency, of the column distance and of the angle γ. We found that $|\underline{v}|/|\underline{v}|^0$ decreases as the angle γ raises, and that it is generally higher for higher values of the speed $|\underline{v}|$ and of the column distance J-I.

Experimentally, the approximate $|\underline{v}|^0$ has also been compared with the value $|\underline{v}|$ obtained from the CCFs fit (taken as un unbiased estimate of the flow speed) for all the data presented in this work (Figures 2–4): the average ratio $|\underline{v}|/|\underline{v}|^0$ ranges from 0.87 to 0.96, suggesting that the blood flow speed can be obtained directly from the peak time of the experimental CCFs in most of the examined cases, thereby simplifying the analysis.

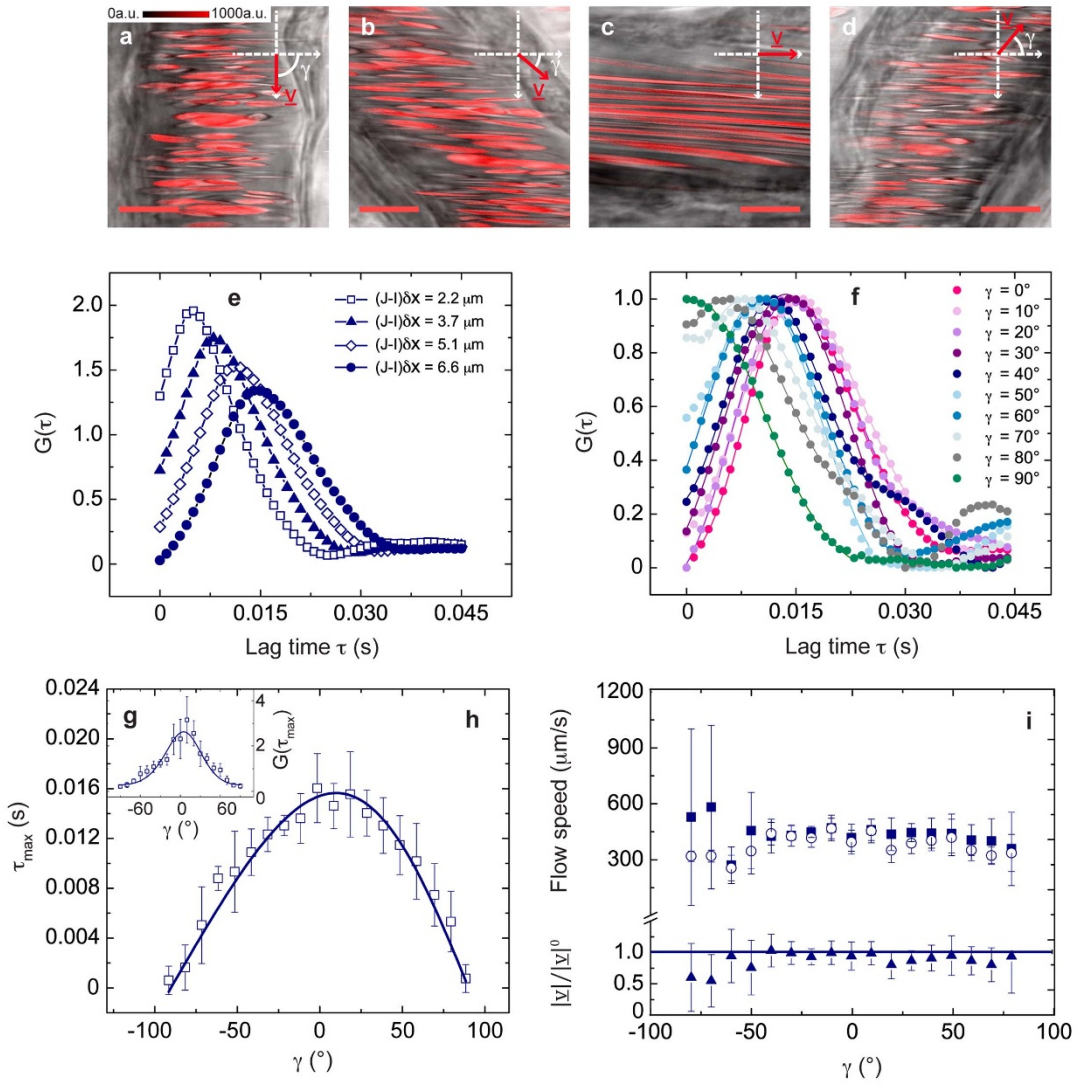

Figure 2 | Validation measurements in Zebrafish embryos (3 days post fertilization d.p.f.). (a)–(d) Confocal xy-images acquired by detecting the fluorescence signal (shown in red) of DsRed-expressing RBCs (λ_{exc} = 561 nm, detection bandwidth = 575–650 nm), overlaid to (non-confocal) transmitted-light images. f_{line} = 1000 Hz, δx = 0.04 μm, scale bar, 10 μm; $\gamma = 90°, 50°, 0°, -50°$ in (a), (b), (c) and (d), respectively. γ and $\underline{v}$ are sketched in the reference Cartesian xy-plane. (e) Exemplifying experimental CCFs for increasing column distance, showing the expected decrease of the peak time for lower *(J-I)δx* values. (f) Normalized CCFs for $\gamma \in [0°, 90°]$ and *(J-I)δx* = 6.6 μm, fitted to equation (3); errors are within the size of data points. (g), (h) Experimental CCF peak amplitude (in g) and peak time (in h) for $\gamma \in [-90°, 90°]$ (mean ± standard deviation (s.d.), from n = 7 *xy*-images), fitted to equation (S.44) and equation (4) (derived in the approximation D = 0 in Supplementary Note 2). Best-fit parameters a = 6.3 ± 0.2 μm in (f) and $|\underline{v}|$ = 424 ± 11 μm/s in (g). (i) Flow speed $|\underline{v}|$ recovered from the CCFs fit (open circles, mean ± s.d., n = 4) and $|\underline{v}|^0$ recovered directly from the CCFs peak time (filled squares, weighted average ± s.d., n = 7). In the lower panel, $|\underline{v}|/|\underline{v}|^0$ is shown for $\gamma \in [-80°, 80°]$. For $\gamma = \pm 90°$, $|\underline{v}|^0$ has not been recovered since the CCF turns into a decay (see panel f).

***In vivo* validation measurements.** The FLICS method has been experimentally validated *in vivo* by blood flow measurements in Zebrafish embryos. This simple organism, in the *Casper* variety, offers several practical advantages (geometrically simple circulatory system, optical transparency and small size) while retaining significant biological relevance due to its widespread use as a model system in cardiovascular[29] and tumor angiogenesis[30] studies.

Confocal raster-scanned *xy*-images have been acquired in the (posterior) caudal cardinal vein of a 3 d.p.f. Zebrafish embryo by detecting the fluorescence signal of the DsRed protein expressed by genetically modified RBCs (Fig. 2a–d). The angle γ has been progressively varied in the range $[-90°; +90°]$ (10° step), and for each value of the angle γ the CCFs have been computed for a fixed column distance *(J-I)δx* = 6.6 μm. This value has been chosen so that the CCF peak is well distinguishable in the whole γ range, since it scales linearly with *(J-I)δx* (Fig. 2e). As predicted by our model (Supplementary Note 2 and Supplementary Fig. 2c), the CCF peak shifts toward shorter lag times when γ increases from 0° to 90° (Fig. 2f) due to a reduction in the slope of the diagonal lines produced by RBCs in raster-scanned images. Equivalently, a decrease of the CCF peak time has been detected for γ in the range $-10° \rightarrow -90°$ (Supplementary Fig. 4). In the whole range $[-90°; +90°]$, the dependence of the experimental CCF peak time and amplitude on γ (Fig. 2g, h) is well described by the analytical expressions derived in Supplementary Note 2 (eqs. 4 and S.44), confirming the validity of the theoretical framework that we developed.

Figure 2i shows the comparison between the flow speed $|\underline{v}|$ recovered from the CCFs fit and the approximate estimates $|\underline{v}|^0$ obtained from their peak time. Within the large explored range for γ, we found an average ratio $|\underline{v}|/|\underline{v}|^0 = 0.87$ (with $|\underline{v}|/|\underline{v}|^0$ as high as 0.99 for a flow direction parallel to the scan path). The recovered velocity values (Fig. 2i) do not depend on the angle γ and lead to an average value

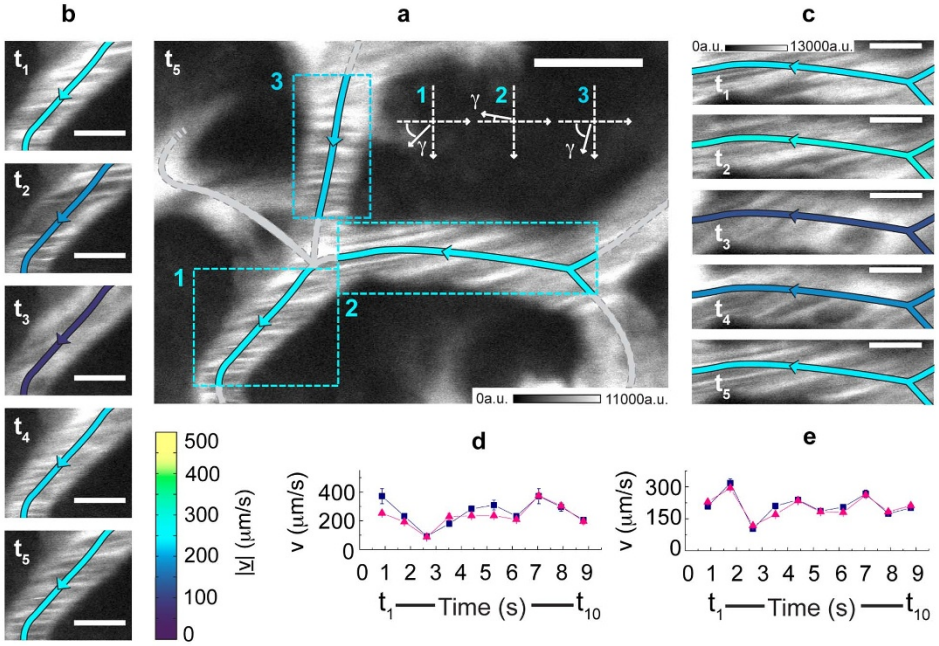

Figure 3 | Measurement in time of the blood flow speed in the hepatic microcirculation. (a) *xy*-image acquired by detecting the photoluminescence (shown in white) of 5-nm QDs (λ_{exc} = 900 nm, detection bandwidth = 640–690 nm); f_{line} = 850 Hz, δx = 0.051 μm, scale bar, 10 μm. CCFs have been derived on the evidenced ROIs (ROI 1: 240 × 210 pixels; ROI 2: 450 × 120 pixels; ROI 3: 145 × 250 pixels) for $(J\text{-}I)\delta x$ = 0.5–2 μm and fitted (equation (3)), leading to $|\underline{v}|$ = 235 ± 4 μm/s, 235 ± 3 μm/s and 229 ± 8 μm/s for ROIs 1, 2 and 3, respectively. A color coding is assigned for the speed $|\underline{v}|$, while the arrows indicate the flow direction. γ, fixed to 50°, −4° and 80° in ROIs 1, 2 and 3, is sketched in the reference *xy*-plane. (b), (c) The *xy*-image in (a) is one out of ten frames of an xyt-stack ($\Delta t = t_{i+1} - t_i = 0.88$ s is the interval between the sampling of the same pixel in two consecutive frames *i* and *i* + 1). The first five frames, each identified by its sampling time $t_i = i\Delta t$, are shown for ROIs 1 (b) and 2 (c). The same color code of panel (a) is adopted for the centreline. Scale bar, 5 μm; same calibration bar (in arbitrary units) in (b) and (c). (d), (e) Estimates for $|\underline{v}|$ (triangles) and $|\underline{v}|^0$ (squares) versus time in ROIs 1 (d) and 2 (e). The average ratio $|\underline{v}|/|\underline{v}|^0$ is 0.92 and 0.95 in ROIs 1 and 2, respectively.

$|\underline{v}|$ = 365 ± 65 μm/s that agrees with the results we obtained by a line-scan method[18] on the same sample (Supplementary Fig. 5) and with the literature[31] for a 3 d.p.f. embryo. The analysis has been performed on a ROI encompassing the whole 1024 × 1024 image. As verified in Supplementary Note 3 and Supplementary Fig. 6, no systematic bias is found on the speed measurement when reducing the number of pixels along both ROI sides.

Measurement of the blood flow speed in the hepatic microcirculatory system. FLICS is not restricted to scan paths parallel to the flow direction. It finds therefore its best application in the *in vivo* measurement of the blood flow velocity in circulatory systems with complex geometry, where the computation of the CCFs is performed on separate ROIs centered on in-focus vessels.

The object of our investigation is the blood velocity determination in the sinusoids (small vessels having a typical ~10 μm diameter) in the hepatic microcirculatory system[32]. 5 nm Quantum Dots (QDs) were intravenously injected in the mouse tail vein to provide contrast with respect to non-fluorescent RBCs. Raster-scanned *xy*-images have been built from the QDs photoluminescence primed by two-photon excitation[33], which allows to explore regions 50–100 μm down in the excised surgically exposed liver. The diagonal lines, alternately produced by photoluminescent QDs and dark RBCs in the *xy*-images, may have low contrast, due to auto-fluorescence contributions and to the scattering processes[34] in a thick living biological sample. In this case, prior to compute the CCFs, a threshold filter should be applied to the ROI excluding the intensity levels below the most frequent signal count. This procedure allows removing the background without affecting the velocity measurement (Supplementary Fig. 7; all images are shown as raw data in the main text, while the filter effect is shown in Supplementary Fig. 8). Upon background removal, the computation of CCFs can be performed either on the QDs signal, as in the present case, or on RBCs upon a LUT inversion; the two procedures lead to equivalent results (Supplementary Fig. 9).

A raster *xy*-image on a 50 × 30 μm² field of view (Fig. 3) has been acquired at subsequent time points, generating an *xyt*-stack that allows to follow the physiological fluctuations of the flow speed over a range of ~tens of seconds. The speed $|\underline{v}|$ has been derived at each time point; an example is shown in Figure 3a where the vessels centreline is depicted with a color coding for the speed $|\underline{v}|$ (arrows represent the flow direction). We are able to accurately follow $|\underline{v}|$ versus time, as shown in Figure 3d, e for two of the investigated vessels, where speed values ranging from 90 to 370 μm/s have been found. These variations can be linked to the slope of the diagonal lines produced in the images by RBCs and QDs (the first five frames t_1–t_5 of the ROIs encompassing the two vessels are shown in Fig. 3b, c). The sensitivity of FLICS to changes in the flow speed has been previously verified *in vitro* (Supplementary Fig. 10).

When studying a larger (110 × 90 μm²) field of view encompassing a highly branched region of the hepatic microvasculature (Fig. 4), many ROIs can be analyzed in parallel. Figure 4a shows a raw *xy*-image at a selected time point, along with twelve ROIs on which CCFs have been derived. Despite the large field of view, the computed CCFs still show the expected peak (Fig. 4c). The estimates $|\underline{v}|$ and $|\underline{v}|^0$, reported in Table 1, are comparable with the speeds recovered in Figure 3. This is a clear indication of the possibility of extending the cross-correlation analysis to raster-scanned *xy*-images irrespectively of the adopted zooming factor. This conclusion is reinforced by the analysis of ROIs 10 and 11, which include the very same vessels examined in Figure 3.

Discussion

We have shown that the FLICS method provides the measurement of the blood flow speed from *single* raster-scanned *xy*-images, acquired

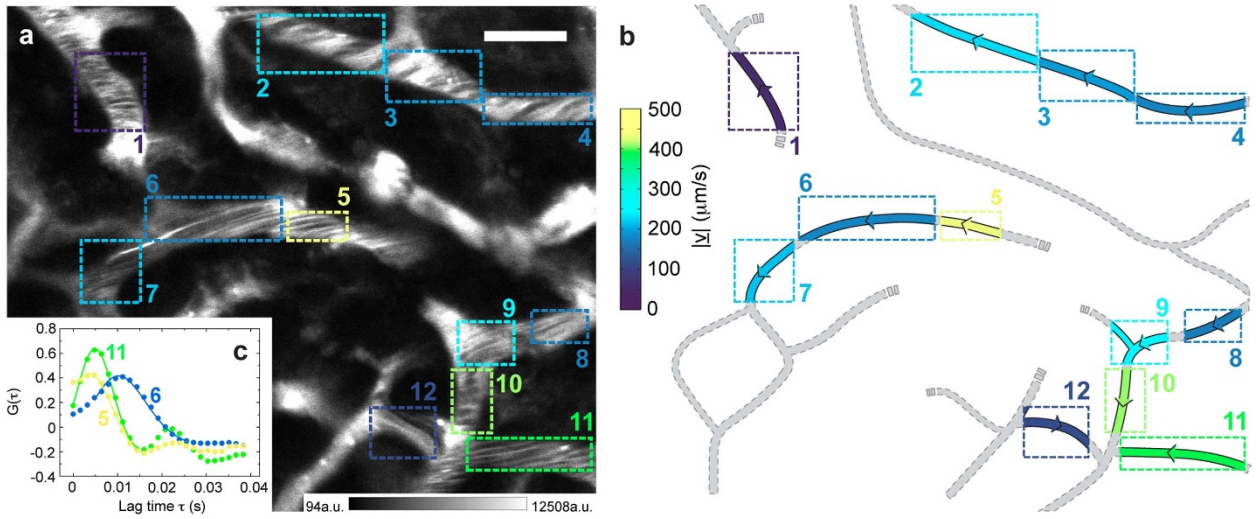

Figure 4 | Measurement of the blood flow speed in the hepatic microcirculation on a wide field of view. (a) xy-image acquired by detecting the photoluminescence (shown in white) of 5-nm QDs ($\lambda_{exc} = 900$ nm, detection bandwidth = 640–690 nm); the lower right corner corresponds to the same region analysed in Figure 3. $f_{line} = 627$ Hz, $\delta x = 0.102$ μm, scale bar, 15 μm. CCFs have been derived on the selected ROIs (~ 100 × 50–200 × 100 pixels) for $(J\text{-}I)\delta x = 0.51$–$2.55$ μm; the estimated $|\underline{v}|$ and $|\underline{v}|^0$, recovered by the fit (equation (3)) and from the peak time (equation (4)) of the experimental CCFs, are reported in Table 1. (b) Schematic of the vessel centrelines for the image in (a). In each ROI, the arrow defines the flow direction and the color codes for the speed value $|\underline{v}|$. Vessels not analysed are shown in grey. (c) CCFs computed for $(J\text{-}I)\delta x = 2.04$ μm in ROIs 5, 6 and 11 (errors are within the size of data points). The fit (equation (3)) led to $|\underline{v}| = 499 \pm 18$ μm/s in ROI 5, $|\underline{v}| = 187 \pm 2$ μm/s in ROI 6 and $|\underline{v}| = 396 \pm 3$ μm/s in ROI 11; as expected, the CCF peak shifts toward shorter lag times as the flow speed increases.

with confocal or two-photon excitation microscopy, offering several advantages with respect to state-of-the-art techniques and correlation analyses. First, FLICS does not require the scan path being parallel to the flow direction, thus allowing to map, at the level of single capillaries, the blood flow velocity in a complex network of vessels with multiple relative orientations, as shown in the hepatic microcirculation. A single scan frequency is required for FLICS analysis, in contrast to recently-developed RVFS[37] (Relative Velocity Field Scanning) and the choice of this scan speed is easily accomplished by live scanning the sample at increasing f_{line} until diagonal lines appear. The scan frequencies of standard commercially available scanning microscopes (10–2000 Hz) are suitable to map blood flows, avoiding the implementation of ad-hoc setups or of resonant scanning heads.

Secondly, compared to tracking based methods[35,36], since a single *xy*-image suffices for FLICS, kinetic studies can be performed in space and time through sequential imaging (*xyt*- and *xyz*-stacks) with a typical time step of the order of 0.5–1 s. This, combined with the high spatial resolution of the exploited images (200 nm in the radial direction, 0.5–1.5 μm in the axial direction), allows to monitor relevant morphological parameters (e.g. vessels diameter and density), simultaneously to the flow speed. Moreover, the impact on the hemodynamics of eventual obstructions can be assessed and the slow deformation dynamics[38] of cells adhering to the vessel walls can be monitored. In particular, the ability to relate the blood flow dynamics in the microcirculation to leukocyte morphological parameters is a hot topic in the study of inflammatory responses, e.g. T cell-mediated liver immunopathology[39]. Efforts are ongoing in applying FLICS to investigate the effect of T cell adhesion to sinusoids walls on the blood flow velocity in healthy and diseased liver.

Methods

Chemicals. Fluorobrite microspheres (Sigma-Aldrich), 1 μm in size, have been used without further purification. For cross-correlation test measurements a borosilicate capillary tube (CM Scientific Ltd., UK) has been used, with a square section of 800 × 800 μm² (40 μm wall thickness). The square section has been chosen to minimize aberrations in the focal volume. The laminar flow of the solutions in the capillary has been obtained by connecting both sides of the capillary tube to 4 cm³ glass cylinders used as sample reservoirs. These cylinders have been set horizontally and at different heights by a micrometric regulation. The flow speed from the upper cylinder to the lower one through the capillary tube can be changed by varying the relative height of the two reservoirs. Surface tension prevents the sample solution from spilling from the cylinders.

Animal models. *Zebrafish embryos.* Validation measurements have been performed on Zebrafish embryos (Danio rerio, 3 days post-fertilization, ~3–4 mm long), belonging to the mutant transgenic line mitfa$^{w2/w2}$;roy$^{a9/a9}$;*Tg(gata1:dsRed)*^{sd2} [40], in which the red fluorescent protein DsRed is expressed by red blood cells. The embryos, in the Casper variety, do not present skin pigmentation and are optically weakly scattering. Zebrafish embryos have been anesthetized in 40 mg/l tricaine (Ethyl 3-aminobenzene methansulfonate, Sigma-Aldrich Corporation), then embedded in lateral position in small microscopic chambers filled with 1.5% low melting point agarose (Sigma Aldrich, A9414-250G). The low tricaine concentration anesthetizes the sample without impairing cardiac functions and heart rate, while the agarose concentration helps in holding it immobilized throughout the measurement. All the experimental protocols have been reviewed and approved by the Institutional Review Board at the Department of Biosciences of University of Milan. They have been conducted in accordance with National and European laws and regulations controlling experiments on live animals.

Mice. C57BL/6 mice have been purchased from Charles River. Mice have been housed under specific pathogen-free conditions and used at 6–8 weeks of age. All experimental animal procedures have been approved by the Institutional Animal Committees of San Raffaele Scientific Institute.

Liver Intravital Microscopy – Surgery. A tail vein catheter (VisualSonic) have been inserted into previously shaved mice prior to anesthetization with 5% isoflurane (Abbot) through a nose cone also delivering oxygen at 1 L/min. Follow-up surgery and liver intravital imaging have been carried out with lower concentrations of isoflurane (between 0.8% and 1%). Continuous body temperature monitoring through a rectal probe has been performed to ensure that a narrow range of 37–38°C is maintained at all times. After opening the skin with a midline incision and detaching peritoneal adherences, midline and left subcostal incisions have been made in the peritoneum through a high-temperature cautery. The falciform ligament has been resected and mice have been placed in a left lateral position with the left liver lobe gently exteriorized onto a glass coverslip attached to a custom-made imaging platform. The liver has been covered with plastic wrap, the incision has been packed with moist gauze, and the imaging platform has been sealed to prevent dehydration.

Liver sinusoids have been visualized by injecting non-targeted 5 nm Quantum Dots 655 (Invitrogen) intravenously immediately prior to imaging.

Optical Setup. *Confocal microscope.* The system is based on an inverted Leica microscope (TCS STED CW SP5, Leica Microsystems, Wetzlar, Germany) equipped with 3 objectives (20×/0.85 AIR, 40×/1.3 and 100×/1.4 OIL), 6 laser lines (458 nm, 476 nm, 488 nm, 514 nm, 561 nm, 633 nm), 2 photomultiplier tubes and 2 high-

Table 1 | Blood flow speed in the twelve ROIs selected in Figure 4. Data refer to the estimates of the flow speed $|\underline{v}|$ provided by the fit of the experimental CCFs, and to the estimates $|\underline{v}|^0$ recovered directly from the peak time of the CCFs (equation (4); each estimate is the weighted average of the values obtained from the peak time of the CCFs computed for four column distances in the corresponding ROI). Apart from ROIs 1 and 10, where the approximate $|\underline{v}|^0$ could not be obtained due to its singularity (see eqs. S.37 and S.39 in Supplementary Note 2), the direct measurement of the flow speed from the CCFs peak time was possible in all the ROIs and led to a 0.96 average ratio $|\underline{v}|/|\underline{v}|^0$

ROI	1	2	3	4	5	6	7	8	9	10	11	12
$\|\underline{v}\|$ (μm/s)	56 ± 5	226 ± 7	187 ± 10	186 ± 3	499 ± 18	187 ± 2	213 ± 1	163 ± 4	239 ± 13	168 ± 8	396 ± 3	137 ± 1
$\|\underline{v}\|^0$ (μm/s)	-	260 ± 39	235 ± 34	168 ± 16	375 ± 73	192 ± 17	203 ± 6	151 ± 12	332 ± 42	-	406 ± 60	138 ± 7

sensitivity Hybrid detectors. The system is provided with both a conventional and a resonant scanning head, allowing a scan frequency range of 10 Hz–8 kHz per line.

The DsRed absorption was primed by the 561 nm solid state laser and the confocal detection was accomplished by a photomultiplier tube (detection bandwidth 575–650 nm). Fluorobrite microspheres have been excited at 514 nm and the emitted signal detected in the range 525–600 nm.

Two-photon microscopy set-up. The setup is based on a commercially available scan head (TriM Scope II, LaVisionBioTec), coupled to an inverted microscope and to a tunable fs-pulsed Ti:Sa laser (680–1080 nm, 120 fs FWHM pulse duration, 80 MHz repetition rate, Ultra II, Coherent). The beam, for its optimization, passes through a beam-shaping device consisting of a pair of crossed polarizers that control the excitation power, a telescope for adapting the collimation of the laser beam and matching the beam dimension to the size of the objective lens back focal plane, and a prism-based chirp compensation unit that compensates for pulse broadening due to the optical components and the objective lens. The beam alignment is checked thanks to four-quadrant photo diodes placed inside the beam-shaping unit and the scan-head. A high working distance objective (NA = 1.0, WD = 1.9 mm, 20× water dipping Zeiss *plan-apochromat* objective) simultaneously excites the sample and collects the emitted signal in backscattering geometry. The fluorescence and second harmonic generation are steered to a non-descanned unit and split into four channels (blue, green, red and far red). Spectral separation is achieved by dichromatic mirrors and bandpass filters (455/50 nm, 525/50 nm, 590/50 nm and 665/50 nm) in front of each photomultiplier tube (3 Hamamatsu H7422-40 GaAsP High Sensitivity PMT, 1 Hamamatsu H7422-50 GaAsP High Sensitivity PMT red extended).

The entire microscope is surrounded by a custom made thermostatic cabinet in which the temperature is kept at 37°C (air thermostating by "The Cube", Life Imaging Services, Basel, CH).

QDs absorption has been primed at 900 nm by the two-photon laser and the fluorescence has been detected through the filter 665/50 nm.

Software. All the acquired images have been visualized and linearly contrast-adjusted using ImageJ (U.S. National Institute of Health, Bethesda, Maryland, USA). The cross correlation functions have been calculated by means of a custom designed Python code based on a Fast Fourier Transform algorithm. The same code has been used to apply the threshold filter to the images. The program OriginPro8 (OriginLab) has been employed for the CCFs fitting.

1. Tuma, R. F., Duran, W. N. & Ley, K. *Microcirculation. Handbook of Physiology.* Second Edition, Elsevier Science (2008).
2. Carmeliet, P. *et al.* Angiogenesis in health and disease. *Nat. Med.* **9**, 653–660 (2003).
3. Jain, R. K. *et al.* Molecular regulation of vessel maturation. *Nat. Med.* **9**, 685–693 (2003).
4. Adams, R. H. & Alitalo, K. Molecular regulation of angiogenesis and lymphangiogenesis. *Nat. Rev. Mol. Cell. Biol.* **8**, 464–478 (2007).
5. Briers, J. D. Laser Doppler, speckle and related techniques for blood perfusion mapping and imaging. *Physiol. Meas.* **22**, R35–R66 (2001).
6. Calamante, F., Thomas, D. L., Pell, G. S., Wiersma, J. & Turner R. Measuring cerebral blood flow using magnetic resonance imaging techniques. *J. Cerebr. Blood F. Met.* **19**, 701–735 (1999).
7. Srinivasan, V. J. *et al.* Quantitative cerebral blood flow with optical coherence tomography. *Opt. Expr.* **18**, 2477–2494 (2010).
8. Macé, E. *et al.* Functional ultrasound imaging of the brain. *Nat. Methods* **8**, 662–664 (2011).
9. Santisakultarm, T. P. *et al.* In vivo two-photon excited fluorescence microscopy reveals cardiac- and respiration-dependent pulsatile blood flow in cortical blood vessels in mice. *Am. J. Physiol. Heart. Circ. Physiol.* **302**, H1367–H1377 (2012).
10. Shih, A. Y. *et al.* Two-photon microscopy as a tool to study blood flow and neurovascular coupling in the rodent brain. *J. Cerebr. Blood F. Met.* **32**, 1277–1309 (2012).
11. Miyawaki, A. Innovations in the imaging of brain functions using fluorescent proteins. *Neuron* **48**, 189–199 (2005).
12. Helmchen, F. & Kleinfeld, D. In vivo measurement of blood flow and glial cell function with two-photon laser scanning microscopy. *Methods Enzymol.* **444**, 231–254 (2008).
13. Kim, T. N. *et al.* Line-scanning particle image velocimetry: an optical approach for quantifying a wide range of blood flow speeds in live animals. *PLOS ONE* **7** (6) (2012).
14. Raffel, M., Willert, C., Wereley, S. & Kompenhans, J. *Particle image velocimety: a practical guide.* Second Edition. Springer-Verlag Berlin Heidelberg New York (2007).
15. Brinkmeier, M., Dörre, K., Stephan, J. & Eigen, M. Two-beam cross-correlation: a method to characterize transport phenomena in micrometer-sized structure. *Anal. Chem.* **71**, 609–616 (1999).
16. Pozzi, P. *et al.* Electron multiplying charge-coupled device-based fluorescence cross-correlation spectroscopy for blood velocimetry on zebrafish embryos. *J. Biomed. Opt.* **19**, 067007 (2014).
17. Pan, X., Shi, X., Korzh, V., Yu, H. & Wohland, T. Line scan fluorescence correlation spectroscopy for three-dimensional microfluidic flow velocity measurements. *J. Biomed. Opt.* **14** (2), 024049 (2009).
18. Rossow, M., Mantulin, W. W. & Gratton, E. Scanning laser image correlation for measurement of flow. *J. Biomed. Opt.* **15**, 026003 (2010).
19. Kleinfeld, D., Mitra, P. P., Helmchen, F. & Denk, W. Fluctuations and stimulus-induced changes in blood flow observed in individual capillaries in layers 2 through 4 of rat neocortex. *Proc. Natl. Acad. Sci.* **95**, 15741–15746 (1998).
20. Driscoll, J. D., Shih, A. Y., Drew, P. J. & Kleinfeld, D. Quantitative two-photon imaging of blood flow in cortex. *Imaging in neuroscience and development* **Vol. 2**. New York: Cold Spring Harbor Laboratory Press, 927–937 (2011).
21. Drew, P. J., Blinder, P., Cauwenberghs, G., Shih, A. Y. & Kleinfeld, D. Rapid determination of particle velocity from space-time images using the Radon transform. *J. Comput. Neurosci.* **29**, 5–11 (2010).
22. Wiseman, P. W., Squier, J. A., Ellisman, M. H. & Wilson, K. R. Two-photon image correlation spectroscopy and image cross-correlation spectroscopy. *J. Micr.* **200**, 14–25 (2000).
23. Digman, M. A. *et al.* Measuring fast dynamics in solutions and cells with a laser scanning microscope. *Biophys. J.* **89**, 1317–1327 (2005).
24. Hebert, B., Costantino, S. & Wiseman, P. W. Spatiotemporal image correlation spectroscopy (STICS) theory, verification, and application to protein velocity mapping in living CHO cells. *Biophys. J.* **88**, 3601–3614 (2005).
25. Coppola, S. *et al.* Quantitative measurement of intracellular transport of nanocarriers by spatio-temporal image correlation spectroscopy. *Methods Appl. Fluoresc.* **1**, 015005 (2013).
26. Rossow, M. J., Sasaki, J. M., Digman, M. A. & Gratton, E. Raster image correlation spectroscopy in live cells. *Nat. Protoc.* **5** (11), 1761–1774 (2010).
27. Wu, B., Chen, Y. & Müller, J. D. Fluorescence correlation spectroscopy of finite-sized particles. *Biophys. J.* **94**, 2800–2808 (2008).
28. Higgins, J. M., Eddington, D. T., Bhatia, S. N. & Mahadevan, L. Statistical dynamics of flowing red blood cells by morphological image processing. *PLOS ONE* **5**, 2, 1000288 (2009).
29. Chico, T. J. A., Ingham, P. W. & Crossman, D. C. Modeling cardiovascular disease in the Zebrafish. *Trends Cardiovasc. Med.* **18**, 150–155 (2008).
30. Tobia, C., De Sena, G. & Presta, M. Zebrafish embryo, a tool to study tumor angiogenesis. *Int. J. Dev. Biol.* **55** (4–5), 505–9 (2011).
31. Shi, X. *et al.* Sensitivity in zebrafish and drosophila embryos by fluorescence correlation spectroscopy. *Dev. Dynam.* **238**, 3156–3167 (2009)
32. Vollmar, B. & Menger, M. The hepatic microcirculation: mechanistic contributions and therapeutic targets in liver injury and repair. *Physiol. Rev.* **89**, 1269–1339 (2009).
33. Helmchen, F. & Denk, W. Deep tissue two-photon microscopy. *Nat. Methods* **2** (12), 932–40 (2005).
34. Caccia, M. *et al.* Image filtering for two-photon deep imaging of limph nodes. *Eur. Biophys. J.* **37** (6), 979–87 (2008).
35. Reyes-Aldasoro, C. C., Akerman, S. & Tozer, G. M. Measuring the velocity of fluorescently labeled red blood cells with a keyhole tracking algorithm. *J. Micr.* **229**, 162–173 (2008).
36. Guo, D., van de Ven, A. L. & Zhou, X. Red blood cell tracking using optical flow methods. *IEEE J. Biomed. Health Inform.* **18**, 991–998 (2014).
37. Kamoun, W. S. *et al.* Simultaneous measurement of RBC velocity, flux, hematocrit and shear rate in tumor vascular networks. *Nat. Methods* **7** (8), 655–660 (2010).
38. Geissmann, F. *et al.* Intravascular immune surveillance by $CXCR6^+$ NKT cells patrolling liver sinusoids. *PLOS Biol.* **3** (4), 0650–0661 (2005).
39. Guidotti, L. G. & Chisari, F. V. Immobiology and pathogenesis of viral hepatitis. *Annu. Rev. Pathol.* **1**, 23–61 (2006).

40. Traver, D. *et al*. Transplantation and in vivo imaging of multilineage engraftment in zebrafish bloodless mutants. *Nat. Immonol.* **4**, 1238–1246 (2003).

Acknowledgments

This work was supported by Academic Funding Unimib 2014 (L.S. and M.C.), MIUR 2008JZ4MLB PRIN project (M.C.), Fondazione Cariplo grant 2010-0454 (G.C.), US National Institutes of Health grant R01-AI40696 (L.G.G.), ERC grant 250219 (L.G.G.), ERC grant 281648 (M.I.), Italian Association for Cancer Research (AIRC) grant 9965 (M.I.) and Career Development Award from the Giovanni Armenise-Harvard Foundation (M.I.).

Author contributions

L.S. and M.B. conceived the technique and the experiments, acquired and analyzed data, wrote the manuscript. M.C., G.C. and L.D. supervised the project and wrote the manuscript. G.C., M.B., L.S. and M.C. derived the theoretical framework. P.P. wrote the Python code. M.I. and D.I. performed mouse surgery and helped in two-photon experiments. M.I. and L.G.G. provided financial support for two-photon experiments. F.C. provided Zebrafish embryos.

Additional information

Supplementary information accompanies this paper at http://www.nature.com/scientificreports

Competing financial interests: The authors declare no competing financial interests.

How to cite this article: Sironi, L. *et al. In Vivo* Flow Mapping in Complex Vessel Networks by Single Image Correlation. *Sci. Rep.* **4**, 7341; DOI:10.1038/srep07341 (2014).